Deutscher Luft- und Raumfahrtkongress 2015, Rostock, Germany, 22nd – 24th September 2015
DocumentID: 370254

IN-FLIGHT REMOTE SENSING AND CHARACTERIZATION OF GUSTS, TURBULENCE, AND WAKE VORTICES

N. Fezans, J. Schwithal, D. Fischenberg,
DLR (German Aerospace Center), Lilienthalplatz 7, 38108 Braunschweig, Germany

Abstract

In this paper, the in-flight remote sensing technologies are considered for two applications: active load alleviation of gust and turbulence and wake impact alleviation. The paper outlines the strong commonalities in terms of sensors and measurement post-processing algorithms and presents also the few differences and their consequences in terms of post-processing. The way the post-processing is being made is detailed before showing results for both applications based on a complete and coupled simulation (aircraft reaction due to disturbances and control inputs during the simulation is influencing the sensor measurements).

1. INTRODUCTION AND MOTIVATION

Aircraft flying into inhomogeneous wind fields experience variations of the aerodynamic forces and moments acting all over the airframe. These variations cause undesired aircraft motions as well as structural loads. In order to alleviate or prevent any threat resulting from the flight into inhomogeneous wind fields, various concrete measures are regularly be taken. For instance, aircraft structures are designed based on the maximum loads that result from standardized design cases and considering an additional safety factor. This corresponds to a robustification of the aircraft design itself. Other measures tackle these issues by modifying the procedures, i.e. where, when, and how the aircraft is used. One example of risk alleviation through the enforcement of procedure is to define a “safe air speed” that shall not be exceeded in the presence of turbulence. Another example is the enforcement of separation minima to alleviate the risk that a given aircraft might enter in the wake vortex of another aircraft.

Both strategies are very effective and have been used for decades. However, these strategies are also having drawbacks, one of which being that they negatively impact the efficiency of the aircraft either by increasing its mass or by leading to longer flight durations. Consequently, quite some research work has been performed in the last decades with the aim of finding new ways to ensure at least the same safety level than with the already existing measures but less deteriorating the overall aircraft efficiency.

There are two main strategies to mitigate these drawbacks: either to have a mean to prevent the flight into these possibly dangerous areas with less conservative-ness or to directly alleviate the consequences of flying through these areas. For both applications, being able to directly measure the wind field through which the aircraft will fly would be of great help. With the first mitigation strategy, a severity assessment of each location inside that area could be made, permitting to avoid the (most) dangerous locations, whereas applying the second mitigation strategy the measurements can be used to directly counteract the effects that will result from flying into these areas. This second strategy is schematically represented in FIG 1. The present paper focuses on the measurement post-processing and required measurement interpretation step. Several technologies can be considered for the in-flight remote measurement of the wind fields. Among these technologies, the Doppler LIDAR sensor seems to be the most suited for the applications considered later and the most often used. Thus, in the following, only the Doppler LIDAR technology is considered.

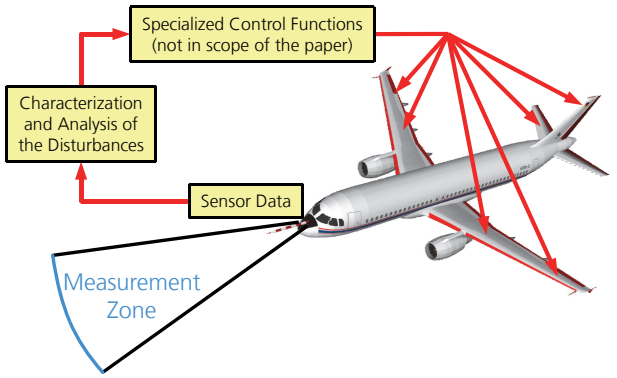

FIG 1: Schematic Representation of the Disturbance Feedforward Impact Alleviation Strategy

This second mitigation strategy (i.e. based on disturbance measurement and alleviation) is the base of two systems called GLAREWISE+TFAC (Gust Load Alleviation using REmote WInd SEnsors and Time-Frequency Allocation Constraints) and OWIDIA (Online Wake IDentification and Impact Alleviation). The focus of this paper lies on the measurement and post-processing steps, which are only the first two steps for both systems. Detailed information on the OWIDIA can be found in [1]. Details on the GLAREWISE+TFAC system will be published soon.

Section 2 presents the Doppler LIDAR sensor measurement principle and the way a simulation model for these sensors can be built and integrated into a nonlinear flight dynamics simulation program. Section 3 presents the general idea behind the sensor measurement post-processing algorithms as well as the numerical algorithms (formulation and resolution) used. Section 4 shows two examples: one for the application to gust and turbulence recognition, and the other for the characterization of wake vortices. The latter example includes the alleviation of the detected wake vortices. Finally, the need for future flight demonstrations of this technology is explained in section 5.

2. DOPPLER LIDAR: MEASUREMENT PRINCIPLE AND SIMULATION MODELS

Doppler LIDAR sensors permit to retrieve relative velocity information based on the Doppler Effect. A laser source is used to illuminate the "objects of interest" which reflect or scatter the laser light back to a detector. The detector is able to detect the slight frequency shifts that result from observing and object located at an increasing/decreasing distance. If the object relative motion is oriented toward the sensor, then the frequency of the backscattered light will be increased (so-called blue shift). On the contrary, if the object is moving away from the sensor, the backscattered light frequency will be lower than the original light frequency (red shift). Using a well-defined wavelength or frequency - as with a laser source - enables the comparison between the original and backscattered light spectrums, which, in turn, permits to determine the change in distance between the sensor and the illuminated object. There are numerous types of detector technologies, whose descriptions go well beyond the scope of the present paper. However, two main distinctions based on some technological differences between the different Doppler LIDAR sensors shall be made. The first distinction can be made on the wavelength used. Some Doppler LIDAR sensors are working in the infrared wavelength domain and are based on the light that is backscattered by small particles in the air (Mie scattering / coherent detection). Other Doppler LIDAR sensors are working in the ultraviolet wavelength domain and are based on the light that is backscattered by the molecule of the air itself (Rayleigh scattering / incoherent detection). This distinction must be made due to the fact that the performance of both technologies can significantly differ and do not depend on the same parameters [2]. The second distinction to be made is between "pulsed" and "continuous wave" LIDARs. In a pulsed LIDAR, the light is emitted during a very short time and as a pulse (duration typical in the order of a few tens of nanoseconds) and the distance at which the measurement is made is determined by the time waited between the pulse emission and the detection (forth and back travel time for the light). With a continuous wave LIDAR the distance information is lost (sometimes not necessary) unless some focusing optics is used to select the "distance of interest" [3], [4]. Further information on remote wind sensing techniques can be found in the very comprehensive DLR report [5] and the PhD thesis [6], which constitute a very detailed reference regarding the LIDAR technology.

This extremely short and simplified explanation for the distinction between the various sensor types can however be ignored for the focus and the considerations of this paper. These properties would impact the quality of the measurements or the exactly measurement geometry, which must be taken into account while designing the algorithm and selecting one particular sensor but the main ideas behind the post-processing algorithms and the measurement interpretation are the same.

Sensor simulation models for use in a flight dynamics simulation program are typically based on two main elements: the simulation of the "perfect" measurement and the "error models". "Perfect" measurement shall not be interpreted here as the measurement that the user would like to have but as the measurement that would be obtained if the sensor hardware did not deteriorate the measurement. For the case of the Doppler LIDAR sensors the perfect measurement is usually determined by the sensor geometry, i.e. where the measurements are made, and the relative wind (aircraft velocity with respect to the air particles at these locations). The location of the measurement is not a point in space but rather a three-dimensional domain. Consequently the measurement corresponds to a weighted-average of the relative wind over this three-dimensional domain, which can be generically represented by considering that the measurement *M* can be expressed as a function of the wind field itself and of a weighting function:

$$M = f(WindField, WeightingFunc: 3Dpos \mapsto weight) \quad (1)$$

The weighting function results from the differences in terms of backscattering energy coming from the different locations inside this domain. Therefore this weighting function and its impact on the measured values strongly depend on the exact sensor configuration. A simplified representation that can be used when no better information is available or to perform relatively generic investigations is to consider the wind field along a segment of the laser beam direction and to take the average wind this segment. As mentioned before the Doppler Effect applies to the change of distance between the observed object and the observer location. This means that only the velocity component in the direction of the laser beam (assuming laser source and detector are the same place) is measured. This direction is commonly called Line-of-Sight direction (LoS). There are some unusual sensor setups that should permit to retrieve other velocity components than the LoS one, which can also be modeled and treated with the same kind of post-processing algorithms, but that will not be considered hereafter for conciseness reasons [3], [4].

When considering only the Line-of-Sight (LoS) component of the wind $\vec{W}$, a simple representation of the effect of the fact that the measurement domain is not a point is to consider a segment S_1S_2 of the Line-of-Sight direction and to compute the average the LoS-wind $\bar{v}_{LoS}$ as follows:

$$\bar{v}_{LoS} = \frac{\int_{S_1}^{S_2} \vec{W}(s) \cdot \vec{u}_{LoS}\, ds}{|S_1S_2|}, \quad (2)$$

where $\vec{u}_{LoS}$ in a unit vector is Line-of-Sight direction. This which can be approximated by taking enough discrete points along the segment S_1S_2.

When flying at a given air speed, the measurement rate (i.e. the number of measurements per time interval) partly determines the average distance between the individual measurements that are performed. The other factors are the measurement geometry (spread left/right and above/below the flight path direction) and the measurement distance. These factors and the dimensions of the three-dimensional domains where each measurement is being performed together define the spatial resolution of the sensor. In the present work, a poor-spatial resolution is considered as an intrinsic property of the sensor configuration and not as an imperfection.

Imperfect measurements and errors occur for instance when the direction of the laser beam does not match the direction that was assumed or configured for this measurement. Similarly, the energy distribution over the three-dimensional domain might not be perfectly known. An uncertainty regarding some time-delays in the processing chain can also be considered as a

measurement location uncertainty. To summarize, all the aforementioned sources of error can be defined as "pointing" or "geometrical" uncertainties. More classical measurement errors such as imperfect measurement or determination of the frequency shift caused by the Doppler Effect can also affect the remote wind measurements. They can result from plenty of different causes, ranging from some small misalignments in the detector optical system to basic noise on the detector photosensitive components. Doppler LIDAR sensors are complex and as for any type of modelling activity, it is crucial to select the right model complexity for the targeted application. Fortunately, it appears that for the present task pretty simple generic measurement error models can be used to test and validate the developed post-processing techniques.

3. MEASUREMENT POST-PROCESSING AND INTERPRETATION

This section focuses on the post-processing of the measurements. First the models used for the post-processing are explained. Then, the required equations (based on the Bayesian estimation theory and more specifically the maximum likelihood estimation method) are derived [7], [8]. Finally additional information relevant for developing a practical application based on the same post-processing techniques is provided. The results obtained by utilizing this post-processing on the two considered applications (active load alleviation and wake impact alleviation) are shown later in section 4.

3.1. Model used for the post-processing

The post-processing algorithms that are considered in the presented work are all considering parameterized models where the parameters are directly connected to the physics of the considered phenomena. Other modelling strategies (e.g. black-box models, neural networks,...) could theoretically be used, but in practice the connection with the physics is very useful to be able to check the plausibility of the results obtained, to build more robust algorithm, and to be able to physically interpret the detected situation. Besides, choosing a model structure is also a way for the engineer to provide the existing domain-specific knowledge on the physical phenomenon at stakes to the post-processing algorithms.

There are two main types of physics-based parameterized model structures that are usually used. The first and most common type of physics-based parameterized model structure is encountered when sufficient knowledge on the physical phenomena has been acquired and that a certain level of abstraction or comprehension for the phenomenon has been reached. In that case, this knowledge can be used to generate simple parameterized models of these phenomena. These models usually correspond to a very good trade-off between representativity (precision) and complexity (number of parameters, complexity of the relationships). This is typically the case that is encountered when trying to detect and characterize wake vortices based on velocity measurements.

Various low-order models of wake vortex velocity distributions have been proposed, e.g. by Burnham and Hallock [9], by Lamb and Oseen [10], by Proctor [11], by Winckelmans [12] or by Jacquin [13]. These models describe the wind vector that is induced by a vortex at a point in space by specifying that this vector is perpendicular to both the vortex core line and the shortest line joining the vortex core line to the point that is considered. The differences between these models lie in the function $V: r \mapsto V(r)$ that relates the distance r between the point considered and the vortex line to the velocity vector magnitude $V(r)$. The mathematical expressions for the tangential velocity distribution functions defined by the aforementioned models are provided in TAB 1.

These models describe the velocity distribution depending on the distance between the vortex line and the considered position. The vector direction is contained in the plane that is perpendicular to the vortex line. This vector is also perpendicular to the line joining the vortex core and the considered position. The flow field induced by a single vortex and based on the Burnham-Hallock tangential velocity distribution model is schematically represented in FIG 2. In this figure, for readability reasons only the wind vectors at some specific positions are shown. It can be seen that the magnitude of the velocity only depends on the distance to the core and that the maximum velocities are reached at/around the core radius.

Name	Function $V: r \mapsto V(r) = \cdots$
Lamb-Oseen	(3) $\frac{\Gamma}{2\pi r}\left(1 - e^{-\beta\left(\frac{r}{r_c}\right)^2}\right)$
Burnham-Hallock	(4) $\frac{\Gamma}{2\pi}\frac{r}{{r_c}^2+r^2}$
Proctor	For $r > r_c$, (5) $\frac{\Gamma}{2\pi r}\left(1 - e^{-10\left(\frac{r}{b}\right)^{3/4}}\right)$ Otherwise, (6) $\frac{1.4\,\Gamma}{2\pi\, r}\left(1 - e^{-10\left(\frac{r}{b}\right)^{3/4}}\right)\left(1 - e^{-1.2527\left(\frac{r}{r_c}\right)^2}\right)$
Winckelmans	(7) $\frac{\Gamma}{2\pi r}(1 - e^{A})$, (8) with $A = -\frac{\beta_i\left(\frac{r}{b}\right)^2}{\left(1+\left(\frac{\beta_i}{\beta_o}\left(\frac{r}{b}\right)^{5/4}\right)^p\right)^{1/p}}$ (9) $\beta_o = 10$, $\beta_i = 500$, and $p = 3$
Jacquin	(10) $\frac{\Gamma\, r}{2\pi\, r_1^2}\left(\frac{r_1}{r_2}\right)^{1-\alpha}\frac{1}{\left(1+\left(\frac{r}{r_1}\right)^4\right)^{\frac{1+\alpha}{4}}\left(1+\left(\frac{r}{r_2}\right)^4\right)^{\frac{1-\alpha}{4}}}$ Typical values: $\frac{r_1}{r_2} = 10$ and $0.4 < \alpha < 0.6$

TAB 1. Common wake-vortex tangential velocity models (further explanation on these models found in references [9], [10], [11], [12], [13], and [14])

The wake of an airplane is composed of two such vortices: one generated at the extremity of the left wing and another one rotating in the opposite direction generated at the extremity of the right wing. The typical flow field of a vortex pair is illustrated in FIG 3.

The various models mentioned previously exhibit some differences in and around the vortex core, but a very similar overall wind field otherwise (see for instance [14]). The large-scale representativeness of these models has been shown over the last decades in many studies (see for instance [15] and [16]).

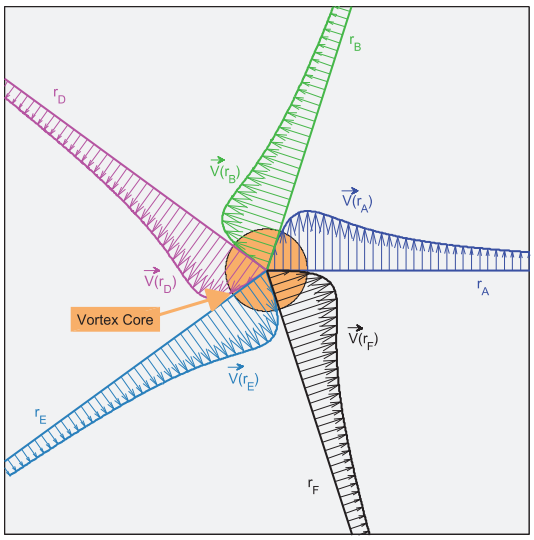

FIG 2: Schematic representation of the flow induced by one vortex alone (model used: Burnham-Hallock).

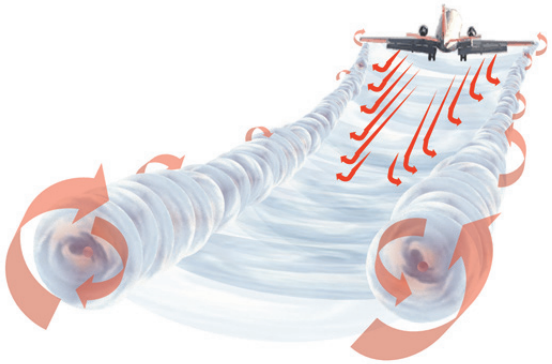

FIG 3: Schematic representation of the flow field induced by an airplane, rotation direction indicated by the arrows.

For other types of phenomena, the level of knowledge or comprehension of these phenomena might not be sufficient to derive simple analytical models. Even when the fundamental physical effects are understood, the nature of the phenomena might also be stochastic, leading to the impossibility to derive such deterministic models. In these cases, a rather commonly used solution is to use a so-called "free-form solution" (second type of physics-based parameterized models): the physical phenomenon is represented by a series of parameters (possibly a very long series) in a given suitable parameter space. For instance, the shape of an object can be represented by a large number of facets: larger numbers of facets implies more freedom and a more precise representation of the object. Another example is the representation of an audio signal by a subset of its frequency components, which is the base of most audio lossy compression algorithms. This latter example is also interesting in the sense that the best audio compression algorithms make use of specific knowledge from the psychoacoustics science to optimize the choice of the combinations of frequency components. This exemplifies that engineers' knowledge can not only be injected in the model structure itself, but also be integrated during the selection of the model parameter values. Finally, a field (regardless whether vector or scalar field) can typically be represented by discretizing the space with some kind of mesh and by representing the local field quantities within the mesh cell or at the mesh node locations. With this approach a three-dimensional wind field is represented by a wind vector (three components) for each node of the mesh. Wind vector values for points that are not directly a mesh node are then retrieved by means of a more or less complicated interpolation procedure. Typically, the parameters that will be searched are the wind vector components at each node, but improvement of the node locations might also be considered in some cases.

This approach has been used to generate a free-form parametric representation of a generic wind field for the modelling of turbulence and gusts. To the best of the authors' knowledge there is no generally applicable model of gusts and turbulence fields. Simplified gust shapes (e.g. the so-called 1-cosine gusts) have been defined to help the comparison between results and to express some certification criteria for structural loads. However, the shapes of the gusts that are encountered in the real world shall not be assumed to match one of these simplified shapes.

For the application to active load alleviation, the fact that the most important short-term wind variations in terms of structural loads are connected to the vertical wind variations, the model can be simplified by considering that only the vertical wind components can change for one node to the other. Similarly, by neglecting the variations between the wind at the left side and at the right side of the aircraft's symmetrical plane the mesh can be drastically reduced and thereby the number of parameters (vertical wind components) that needs to be determined. The same simplification can be made for the local wind variations between two points located on one vertical line. The mesh also can and should be restricted to the area (in space) of interest. Once again, all these ways of reducing the free-form model formulation should be understood as means to integrate engineering judgement into the model structure. Finally, the strongly simplified mesh that has been used for the results on gust and turbulence remote sensing and on characterization presented later in this paper have been obtained with this simplified mesh. This mesh is schematically represented in FIG 4.

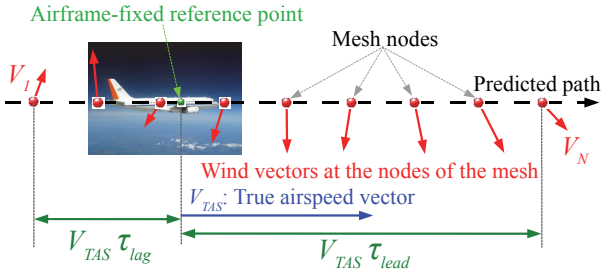

FIG 4: Illustration of the simplified free-form wind field model based on a one-dimensional mesh.

The free-form model structure used in this case is consequently reduced to a set of points defined along the predicted aircraft path: the vertical wind components at these points $(P_i)_{i\in[\![1,N]\!]}$ define the simplified wind profile. The exact mathematical formulas that define the two extreme mesh points as well as all points in between are:

(11) $P_1 = P_{ref} - V_{TAS}\,\tau_{lag}$

(12) $P_N = P_{ref} + V_{TAS}\,\tau_{lead}$

(13) $\forall i \in [\![2, N-1]\!],\ P_i = P_1 + \frac{i-1}{N-1}\overrightarrow{P_1P_N}$.

Typical values for the parameters shown in FIG 4 and in Equations (11-13) are: $1\ s < \tau_{lead} < 2\ s$, $\tau_{lag} = 0.5\ s$, and $N \approx 30$. This corresponds to a trade-off between the

sensor range characteristics, the number of optimization variable (see following sections), and the need to include several nodes behind aircraft's current position (see section 4.1).

3.2. Post-processing via maximum likelihood

The goal of the post-processing is typically to interpret the measurements made such that the entire wind field is reconstructed. In practice only restricted information has been gathered through the measurements. Indeed, in both applications the most important wind directions are the vertical wind components. In the case of gust and turbulence they are one of the main causes for structural excitation and loads. In the case of the wake vortex encounter, the difference of vertical wind along the wing span is the main cause for the additional rolling moment and vertical load factor. These vertical wind components cannot directly be measured, which means that the wind field at locations and directions that were not directly measured needs to be reconstructed. This reconstruction is necessarily is partly a guess that is made based on the surrounding measurements, the engineers' knowledge, and some mathematical tools.

The measurements are usually noted with the letter z and indices are used to distinguish them. Let n be the number of measurements currently contained in the database (or buffer). Then, let

(14) $(z_i)_{i\in[\![1,n]\!]}$

be the n-tuple of measurements. Let $\Theta = [\theta_1, \theta_2, \dots, \theta_p]$ be the vector of all p wind field model parameters. For a given vector $\widetilde{\Theta}$ the n model outputs $(\tilde{y}_i)_{i\in[\![1,n]\!]}$ corresponding to the measurements made (same location and conditions) can be computed and compared to the measurements $(z_i)_{i\in[\![1,n]\!]}$. The closer the measurements and the corresponding model outputs, the more likely it is that the model used and the parameter values used are right. More formally for each measurement and each model parameter vector value, a probability density function (pdf) $x \mapsto p(x|\Theta)$ can be defined by the engineer to represent its belief regarding the measurement under the assumption that these model parameters are right.

For the sake of the explanation, consider a simple system being a solid with a given mass m whose mass will be measured using a scale and the relationship between mass and weight: $P = mg$. If the gravity field is perfectly known the measured mass is only affected by the sensor uncertainty/error of the scale. The error usually has several sources (calibration errors, nonlinearities, quantization, etc.) and can usually be characterized. If the model expressed by the equation $P = mg$ is uncertain (e.g. the equation is approximated or the gravity field itself is uncertain), these model errors and the pure sensor errors combine to form the "measurement error". By describing the stochastic properties of each error source, a model of this measurement error can be derived or estimated. This model describes how likely it is to obtain a given measurement value (here the mass that is deduced from the weight measurement and the model equation) provided a given set of system parameters (here the true mass), which can naturally be written as the pdf:

(15) $measurement \mapsto p(measurement \mid system\ parameters)$

Taking the notations introduced earlier, the pdf that interests us is the following one:

(16) $(z_i)_{i\in[\![1,n]\!]} \mapsto p\big((z_i)_{i\in[\![1,n]\!]} \mid \Theta\big)$.

In many cases, it can be assumed that the error on each measurement does not depend on the other measurements or that:

(17) $\forall i \in [\![1,n]\!],\ p(z_i|\,\Theta) = p\big(z_i \mid \Theta\,,\,(z_j)_{j\in[\![1,n]\!]-\{i\}}\big)$,

and in that particular case:

(18) $p\big((z_i)_{i\in[\![1,n]\!]} \mid \Theta\big) = \prod_{i=1}^{n} p(z_i \mid \Theta)$.

Note that this assumption is often satisfied with noise and quantization effects, but usually not when some sensor calibration biases or model uncertainties are present.

When the aforementioned assumption is made and when additionally assuming that the pdf of each measurement z_i is (or is assumed to be) Gaussian with mean ξ_i and standard deviation σ_i, i.e. reads

(19) $\forall i \in [\![1,n]\!], p(z_i \mid \Theta): z_i \mapsto \frac{1}{\sqrt{2\pi}\,\sigma_i} e^{-\frac{1}{2}\frac{(z_i-\xi_i)^2}{\sigma_i^2}}$,

then the pdf $p\big((z_i)_{i\in[\![1,n]\!]} \mid \Theta\big)$ reads:

$$\begin{aligned} p\big((z_i)_{i\in[\![1,n]\!]} \mid \Theta\big) &= \prod_{i=1}^{n} p(z_i \mid \Theta) \\ &= \frac{1}{(\sqrt{2\pi})^{\,n}\prod_{i=1}^{n}\sigma_i} e^{-\frac{1}{2}\sum_{i=1}^{n}\frac{(z_i-\xi_i)^2}{\sigma_i^2}}. \end{aligned} \quad (20)$$

Regardless of the exact pdf $p\big((z_i)_{i\in[\![1,n]\!]} \mid \Theta\big)$ that is derived for the problem considered, the maximum likelihood estimation method defines the "most likely parameter vector" $\widehat{\Theta}$ as the parameter combination that maximizes the likelihood to have obtained the measurement set $(z_i)_{i\in[\![1,n]\!]}$ that was indeed obtained. This can mathematically be formalized as:

(21) $\widehat{\Theta} = \operatorname{argmax}_{\Theta}\Big(\Theta \mapsto p\big((z_i)_{i\in[\![1,n]\!]} \mid \Theta\big)\Big)$.

Note that the notation p and the abbreviation pdf (probability density function) might lead to think of the functions and values mentioned before are "probabilities". In a strictly mathematical sense, they are however not the probabilities or pdf themselves but beliefs on what these probabilities or pdf would be. The detailed explanation on this as well as the exact differences can be found in the literature on Bayesian estimation (see for instance [7] or [8]) and will therefore not be reminded hereafter.

Quite often, instead of maximizing directly the likelihood function $\Theta \mapsto p\big((z_i)_{i\in[\![1,n]\!]} \mid \Theta\big)$, this function is modified in a way that does not modify the location of its maximum. For instance, by taking the logarithm of a function f with positive values (i.e. $\forall x, f(x) > 0$) it can be shown that $\operatorname{argmax}_x \ln\big(f(x)\big) = \operatorname{argmax}_x f(x)$. Regardless of the function f considered, the function obtained by composing f with a strictly increasing function (which is the case for $\ln$) always satisfies this property. This kind of transformations is often made to simplify the computation of the cost function (and possibly its derivatives) or to improve the conditioning of the optimization problem. For instance, by composing the function of Equation (19) with the Neperian logarithm it can be shown that maximizing the resulting function:

$$\begin{aligned} \ln\Big(p\big((z_i)_{i\in[\![1,n]\!]} \mid \Theta\big)\Big) &= \sum_{i=1}^{n} \ln\big(p(z_i \mid \Theta)\big) \\ &= \sum_{i=1}^{n} \ln\left(\frac{1}{\sqrt{2\pi}\,\sigma_i} e^{-\frac{1}{2}\frac{(z_i-\xi_i)^2}{\sigma_i^2}}\right) \\ &= -\sum_{i=1}^{n}\big(\sqrt{2\pi}\,\sigma_i\big) + -\frac{1}{2}\sum_{i=1}^{n}\frac{(z_i-\xi_i)^2}{\sigma_i^2} \end{aligned} \quad (22)$$

For constant and known standard deviations $(\sigma_i)_{i\in[\![1,n]\!]}$ finally leads to the equivalent least-squares problem:

$$\begin{aligned}\widehat{\Theta} &= \operatorname{argmax}_\Theta\left(\Theta \mapsto p\left((z_i)_{i\in[\![1,n]\!]} \mid \Theta\right)\right)\\ &= \operatorname{argmax}_\Theta\left(\Theta \mapsto \ln\left(p\left((z_i)_{i\in[\![1,n]\!]} \mid \Theta\right)\right)\right)\\ &= \operatorname{argmin}_\Theta\left(\Theta \mapsto \sum_{i=1}^{n} \frac{(z_i-\xi_i)^2}{\sigma_i^2}\right)\end{aligned} \quad (23)$$

This property can be exploited by using specialized optimization algorithms (e.g. Gauss-Newton) which can usually converge significantly faster than the non-specialized algorithms (see [17] and references therein). On well-conditioned maximum likelihood problems (and which do not exhibit local minima) most optimization algorithms should normally find the right parameters, the main difference between the algorithms will in that case only be the computation time needed to converge.

3.3. Measurement data and metadata handling

In the previous section, the measurement set considered for the maximum likelihood estimation was simply noted $(z_i)_{i\in[\![1,n]\!]}$. In practice, there are usually the raw measurement data (i.e. what was written here as z_i) but also the corresponding metadata. In the example of the Doppler LIDAR sensor measurements, the measurements are the measured Line-of-Sight velocities and the corresponding metadata consist of: the measurement location (not just a point, cf. section 2), the Line-of-Sight direction at measurement time, the sensor's own velocity at measurement time, and possibly others depending on the level of detail of the model (e.g. laser pulse power, backscattering coefficients, etc.). The metadata are crucial to be able to define the likelihood functions corresponding to the data.

Sensors might be able to produce several measurements simultaneously or only sequentially, which brings two main post-processing options: a series of "one-shot" estimations based on a subset of relevant measurements or a recursive estimation process computing each time a new estimate based on the previous one and the new measurement(s). Good recursive estimation processes are often (but not always) less computationally expensive (computation time, memory requirements) but defining a good trade-off between robustness and complexity can be very difficult strongly nonlinear relationships between parameters and measurements. The quality of the estimate is also difficult to define in these cases and the estimated error-bounds (e.g. Cramer-Rao) shall not be overinterpreted and always considered with very great caution.

The "one-shot" estimation forces to maintain some kind of "measurement database" containing both the data and the associated metadata and to manipulate and compute more complex mathematical expressions during the estimation process. However, relatively easy metrics can be used for the obtained goodness of fit between the model with the current parameters and all the measurements stored in the database. Here the engineers can integrate their domain-specific knowledge and define what they consider to be a match that provides great confidence in the result and what not. Analyzing the plausibility of the result and the level of confidence with which this result can be used in further steps is crucial to ensure that under no condition the overall system will perform undesired or hazardous actions.

In all systems and applications considered here, the model is strongly nonlinear and the system shall be considered as safety-critical. Consequently, the "one-shot" estimation process has been preferred to the recursive estimation techniques.

3.4. Numerical formulation and resolution

In the various applications considered hereafter, the assumptions mentioned in section 3.2 and leading to the formulation of the equivalent least-squares problem of Equation (23) were made. The model used for the gust and turbulence characterization application was the free-form model structure presented in FIG 4 for which the wind velocities at each node must be reconstructed from the measurement.

The model used for the characterization of wake-vortices was a pair of parallel vortices with the Burnham-Hallock tangential velocity distribution models. The scenarios considered are only based on wake vortices that are "young enough" to not be strongly deformed as this typically happens in later stages of the wake vortex decay [18], [19], [20]. Simplified models of older wake vortices have been developed and used in various studies [21], [22], [23] and [24]. Such models could be used in future versions of the OWIDIA system.

With the model used here, the parameters to be determined are the wake vortex circulation Γ, the distance between the vortex lines b, as well as the three-dimensional orientation of these wake vortex lines relative to the aircraft. As shown in the paper [1], but not reminded hereafter several formulations for this orientation have been used in the authors' previous studies, but besides slight differences in terms of computational cost these formulations are in the end equivalent and straightforward variable changes permits to convert one into the other.

The corresponding maximum likelihood problems were numerically solved with gradient-based local optimization algorithms. The "online" resolutions (i.e. coupled with a full flexible or rigid aircraft simulation program comprising also a flight control system) have usually been performed with a modified Broyden-Fletcher-Goldfarb-Shanno (BFGS) quasi-Newton algorithm. The modification with respect to the standard version consists in using an iterative resolution (with a restricted number of iterations) of the linear problem leading to the new step direction and initial length (before applying a line search). Even though no formal demonstration was attempted, this modification seems to avoid computing very inappropriate descent steps when the Hessian matrix is not well shaped/conditioned (yet), while not impairing the overall convergence property of the algorithm.

As already mentioned, other algorithms could be used for the resolution: the work performed until now focused rather on the physical modelling and the extensive testing in a highly representative simulation environment than on the search for shorter computation time. Nevertheless, the model outputs (in the present case wind velocities at given locations for various sets of parameters) need to be evaluated very often during the process.

Consequently, the time spent evaluating the model outputs is the driving parameter for the overall computational cost and consequently efficient implementations of the model shall be used. For a free-form model as used for the characterization of gust and

turbulence fields, it is crucial to use data structures permitting efficient determination of the nodes and weightings that are needed to evaluate the wind field at each point. Mesh modification operations (e.g. insertion, deletion, or even deformation) have only a very little impact on the computational cost and therefore can be implemented with greater focus on flexibility and modularity than on pure performance.

The cost of evaluating a simple wake vortex model such as the Burham-Hallock one is significantly lower than for the Proctor, Winckelmans, and Jacquin models. This constitute a major advantage in an online wake vortex characterization algorithm, whereas the benefits of these models (possibly higher representativeness around the vortex core region) for this type of online algorithm is rather unclear and expected to be low.

For the application to the characterization of gust and turbulence using a free-form model, it was also found useful to add a Tikhonov regularization term to the least-squares function, which lead to solve the following optimization problem:

$$\widehat{\Theta} = \operatorname{argmin}_{\Theta}\left(\Theta \mapsto \sum_{i=1}^{n} \frac{(z_i-\xi_i)^2}{\sigma_i^2} + \alpha \left\|\check{\Gamma}\,\Theta\right\|^2\right). \quad (24)$$

The Tikhonov matrix $\check{\Gamma}$ shall not be confused with the wake vortex circulation Γ of the application to wake vortex characterization. The used Tikhonov regularization matrix is of size $(p-2)\times p$ with p being the number of parameters in the vector Θ and penalizes the second derivative of the reconstructed wind profile based on the coefficients $[-1,+2,-1]$ of the well-known Mexican Hat wavelet / convolution filter (also called Laplacian-of-Gaussian filter) [25] of order two. The coefficient α permits to tune the relative strength between the Tikhonov penalization and the least-squares criterion. It was found that small values of this coefficient α (not massively changing the shape of the profile found on typical wind profiles) were already well penalizing nonsmooth profiles and also helping the algorithm to converge more quickly.

4. RESULTS ON BOTH GUST AND WAKE-VORTEX CHARACTERIZATION SCENARIOS

4.1. Results of the application to gust characterization

The application presented hereafter was performed within the framework of the EU JTI Smart Fixed Wing Aircraft (SFWA) project. The final goal of the investigated system was the active load alleviation of gusts and turbulence. For this various technologies and control strategies have been investigated. One of the components or subsystems considered was based on a Doppler LIDAR sensor with which the disturbances are recognized slightly before encountering them. This permits to anticipate (near) future loads and to achieve higher alleviation performance than what can be achieved without anticipation. This idea is not new and previous work in this direction has been performed, see for instance [26], [27], [28], [29], [30], and [31]. The Doppler LIDAR post-processing techniques shown in the present paper represent a very significant improvement compared to the corresponding solutions proposed in these previous works.

In the following, the wind reconstruction results are presented. The way the load alleviation itself is performed (based on this reconstructed wind) is not presented but will be published in the near future.

In order to illustrate the way the wind reconstruction is being performed a simple example is used hereafter. In this example, the aircraft is encountering a well-formed analytical 1-cosine vertical gust. This gust is defined with respect to a geodetic reference frame and is fixed in this frame. Since the aircraft is flying almost at constant air speed, this case does not really differ from the way discrete gusts (as defined in the paragraph CS 25.341 of the CS 25 certification specifications [32]) are usually considered either in the time or in the frequency domain. The definition as a “space-fixed” gust is useful to perform the Doppler LIDAR measurement simulation, which requires a complex access to the “real” wind field in order to be able to produce the simulated measurements which will be the starting point for the gust wind reconstruction algorithm.

In this application the lead-time τ_{lead} was set to 1.6 seconds, the lag-time τ_{lag} set to 0.5 seconds, and the number of nodes of the 1-dimensional mesh set to 33. The computation time for the wind reconstruction with a 32-bit single-threaded implementation which was not optimized for speed but for flexibility was between 0.25 and 0.35 seconds on a regular Intel i7-2600 at 3.4 GHz. The variability of the execution time is mainly due to the measurement method which was based on the system clock on a non-real-time environment (Windows 7 Enterprise 64-bit). Another source of slight variation of the execution time is that the quite tight convergence criteria can be reached with less than the maximum allowed number of iterations. Note that the worst-case number of operations and thus the maximum execution time in a real-time environment is bounded. The estimation process was started every 0.3 seconds during the simulation, which means that the current implementation is not running fully in real-time at the moment, but is very close to it. As already mentioned the model outputs computation is by far the largest cost. These computations can be easily fully parallelized such that with the appropriate hardware, there should be no issue to implement a real-time version even if a significantly higher number of nodes would be used.

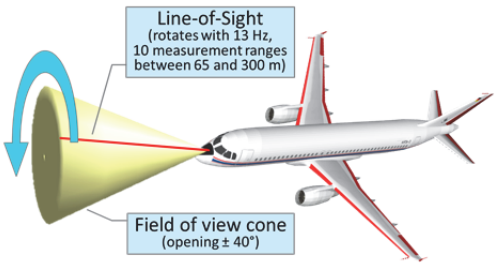

FIG 5: LIDAR sensor scan pattern used for gust and turbulence load alleviation application

The Doppler LIDAR measurement geometry chosen for this application is based on a simple scan mechanism which let the laser beam describe a cone in the aircraft-fixed frame as shown in FIG 5. The Line-of-Sight rotates continuously and measurements are performed at various ranges between 65 and 300 m.

FIG 6 and 7 present the comparison between the true vertical wind (light red) and the reconstructed wind profiles obtained successively during the encounter simulation (dark blue). Both figures present the exact same results: FIG 6 shows all wind profile results superimposed and permits to see the consistence of the estimation over time,

whereas FIG 7 shows the evolution of the wind profile estimates with 300 ms delay between the respective computations. The overall match between true and reconstructed wind is very good and information that is relevant for load alleviation purposes can obviously be extracted from this reconstructed wind profiles.

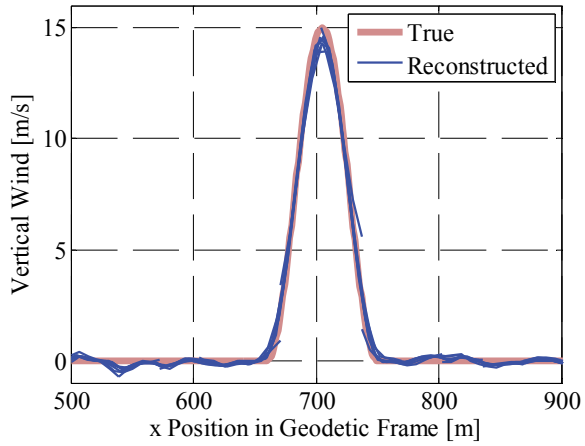

FIG 6: Comparison between the true vertical wind (light coral red) and the reconstructed wind profiles obtained successively during the encounter simulation (blue)

Slight reconstructed vertical wind variations can be observed, especially in the absence of significant vertical wind variations (i.e. before and after the gust). These variations are the consequences of the measurement noise, which is propagated throughout the estimation process and finally slightly impairs the estimation quality. Note that the different wind profiles obtained successively exhibit almost the same deviations with respect to the "true" profile, such that the different blue lines can hardly be distinguished in FIG 6. Each wind profile estimation process was started with the same initial profile, which corresponds to no wind at all. As a consequence, the fact that very similar wind profiles (including the deviations from the true one) have been found cannot result from a reuse of the previously found wind profile. The explanation of the similarity between the results comes from the fact that successive runs of the algorithm use a similar set of measurements. Most of the measurements are the same between both runs. Only a few older measurements were dropped and a few new measurements were added.

In FIG 7, it can be noticed that the extremities of the reconstructed profiles often deviates slightly from the true profile and the expectations or hopes that can be formulated for the wind reconstruction module. The Tikhonov regularization that was introduced to ensure the preference for smooth wind profiles and to improve the convergence of the algorithm causes these deviations at the boundaries of the domain. The two first and two last nodes of the mesh are affected and must be either corrected via an additional post-processing step or simply be ignored for further computation steps. This fact is the main motivation for using a mesh that contains nodes located behind the aircraft as it can be observed in FIG 4: thanks to this configuration the current aircraft position is always sufficiently far from the mesh boundaries to prevent the reconstructed wind at the aircraft location to be affected by the above described effect.

All developments made for the application to the gust and turbulence characterization were made with the aim of using the reconstructed wind profile in a feedforward load alleviation function. The Doppler LIDAR sensor spatial resolutions that can be assumed for near future applications are relatively low and the noise levels to be expected are quite high, such that the reconstructed wind profile information is significantly more trustworthy for large amplitude variations at low frequencies than for lower amplitude variations or higher frequencies. Consequently the developments focused on designing a particularly robust and effective characterization and load alleviation function for this type of disturbances (large amplitudes, low frequencies). Note that these disturbance characteristics are also the ones for which the anticipation capability of the remote wind sensor are most suited in combination with a feedforward load alleviation concept. With the sensor properties that can be assumed for Doppler LIDAR sensors, it would not really make sense to design a load alleviation system based only these sensors. Techniques and systems for structural damping and disturbance rejection for all other types of disturbances should also be added with a complementary function or term (e.g. based on other available sensors distributed over the airframe).

The use of a feedforward gust and turbulence load alleviation function that is capable of anticipating the near future disturbances, in addition to a more classical active load alleviation controller, would permit to greatly reduce the peak structural loads. The wind reconstruction results based on the LIDAR sensors are very promising and should be sufficient to enable the design of such an anticipation-capable feedforward load alleviation function.

4.2. Results of the application to wake-vortex characterization

The application of the remote wind sensing and of the corresponding post-processing to the characterization of wake vortices presented here is part of a larger system, whose objective is to alleviate the impact of wake vortices. Wake vortex encounters can lead to dangerous aircraft reactions with in particular sudden and strong wake-induced rolling motion. The goal of the complete control system called "OWIDIA" (Online Wake IDentification and Impact Alleviation) is to minimize the wake-induced aircraft motion. The concept of the OWIDIA system is shown in FIG 8 and described in detail in [1]. The LIDAR sensor measures the wind velocities in a short distance in front of the aircraft. An Online Wake Identification (OWI) algorithm is applied to reconstruct the wake vortex disturbance by estimating the most-likely parameters of a Burnham-Hallock wake vortex model considering the measured wind velocities. The principle of OWI was developed in [33], [34], [35] and extended in [1]. The OWI component is the measurement post-processing algorithm of the OWIDIA system, which is based on the ideas and elements presented earlier in section 3.

On the basis of the wake vortex that was identified by the OWI, the WIAC (Wake Impact Alleviation Control) module, previously published in [35] and [1] and not described in detail hereafter, determines the wake-induced moments affecting the aircraft and generates control commands that countervail these moments. These commands are added to the commands of the basic flight control system, independently from the control mode that is currently active. In all results shown hereafter the basic flight control system of the A320 is always active: in manual flight mode (autopilot disengaged) and in normal law.

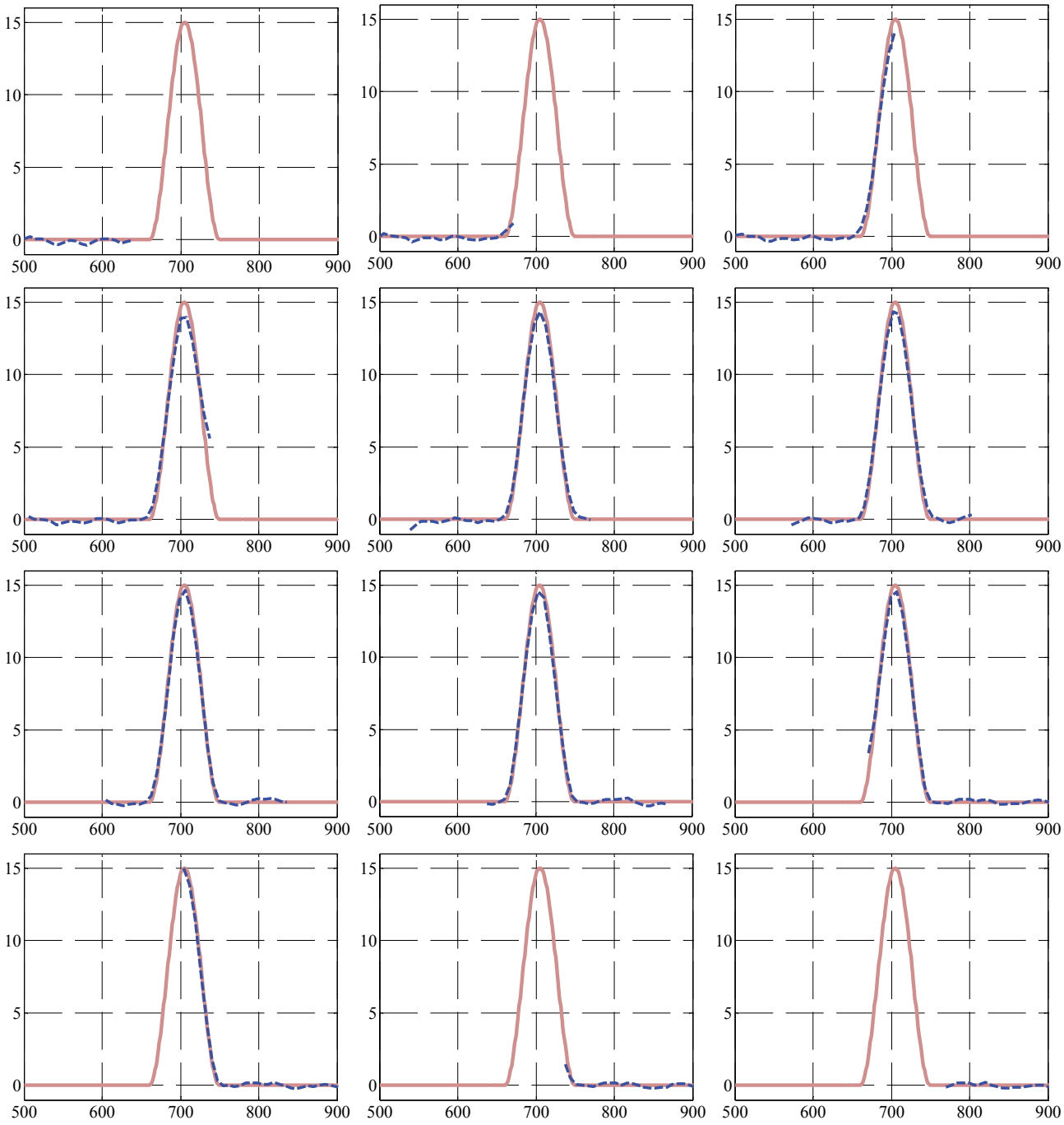

FIG 7: Wind profile after each execution. Axes as in FIG 6: vertical wind in m/s versus geodetic position in meters. Light coral red line represents the “true profile” and the dashed-blue line the reconstructed profile.

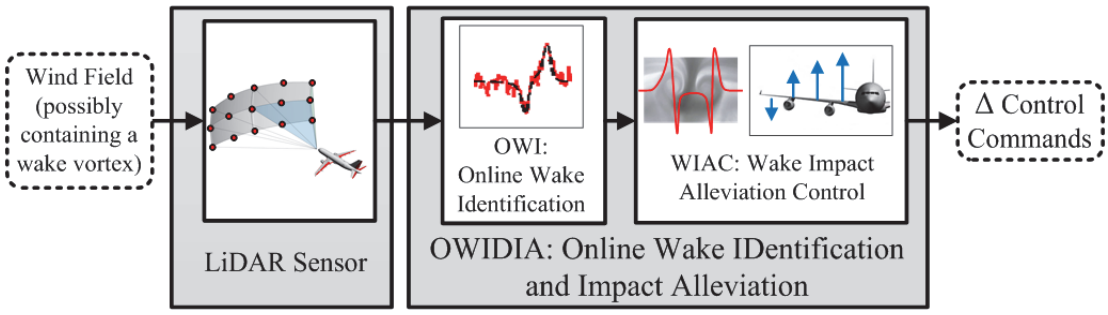

FIG 8: Schematic representation of the Online Wake IDentification and Impact Alleviation (OWIDIA) system.

The overall performance of the system is strongly dependent on the characteristics of the LIDAR measurement. As the control surface deflections commanded by the OWIDIA system are generated directly on the basis of the identified flow disturbances, a poor match of the wake vortex model with the actual wake disturbance strongly impairs the alleviation of the wake-induced aircraft response and in the worst case even can lead to an increased aircraft reaction. An extensive parameter study analyzing the sensitivity of the wake impact alleviation performance with respect to different parameters of the LIDAR sensor was presented in [1]. The scan pattern of the LIDAR sensor assumed in this study differs from the scan mechanism considered for the gust characterization application in section 4.1. Instead of scanning a cone, the LIDAR sensor measures the wind velocities a measurement points at a fixed range. Consequently the measurement point locations are distributed on a sphere whose center is at the sensor location as illustrated in FIG 9. The Line-of-Sight directions were defined based on a lateral and a vertical scan angles $\Delta\Psi$ and $\Delta\Theta$. The respective lateral and vertical angles of view Ψ_{scan} and Θ_{scan} are parameters of the sensor system. A regular grid (i.e. regular steps for $\Delta\Psi$ and $\Delta\Theta$) was used to define the Line-of-Sight directions within the sensor angles of view.

The differences between the used scan patterns between both applications is not the result of a particular optimization of these scan patterns for each application, but rather an indirect consequence of having developed both applications in different projects. OWIDIA was not tested with the cone-shape scan motion and the feedforward active load alleviation was also not tested with the pattern of FIG 9. The blur depth defines the length of measurement domain (cf. section 2), which is called “measurement point” hereafter for the sake of simplifying the wording used.

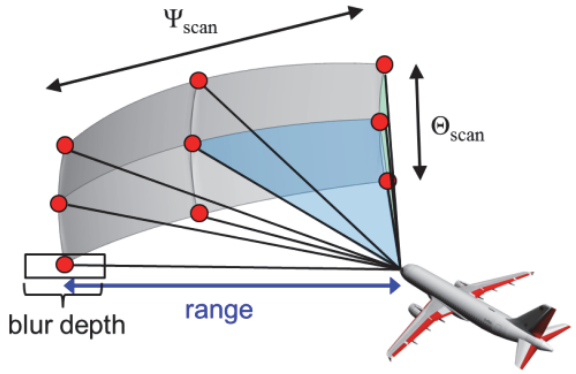

FIG 9: LIDAR sensor scan pattern used for the wake vortex application (3x3 measurement points here)

Different sets of adequate LIDAR parameter combinations could be identified for the considered encounter scenarios in [1], with which the OWIDIA system can reduce the maximum bank angle during the wake vortex encounter by 60-70%. That means that the maximum bank angle the aircraft experiences during the whole simulation (which includes the flight through the wake vortex) when the OWIDIA system is active is 60-70% lower than the maximum bank angle for the same encounter when OWIDIA is not applied.

In the parameter analysis of [1], only a very limited number of encounter scenarios with a wide range of different LIDAR parameters were considered because the purpose was to get some insight into the sensitivity of the system performance with respect to the LIDAR parameter values. Apart from the LIDAR parameter variations, four different lateral encounter angles between the vortex centerline and the aircraft flight path (i.e. 5°, 10°, 15° and 30°) were simulated. The vertical offset between the vortex centerline and aircraft flight path was always 2 m. A positive altitude difference means that the vortex centerline is located above the center of gravity of the aircraft. Recent analysis results show that this small altitude offset represents a favorable encounter geometry because the wake vortex is located approximately in the center of the field of view of the LIDAR measurements. If the altitude offset between the wake vortex and the aircraft is varied, the OWIDIA performance in terms of maximum bank angle reduction also shows strong variations. FIG 10 shows the reduction of the maximum bank angle (during the whole encounter duration) for horizontal wake vortex encounter (i.e. vortex is horizontal and aircraft initial flight path is also horizontal) with 5° lateral encounter angle and different vertical positions of the wake vortex with respect to the aircraft applying a 3x3 measurement point scan array. In both cases, when the OWIDIA system is active (red crosses) or inactive (blue circles), the basic control system of the aircraft, which corresponds to the normal law of an Airbus A320, is active. The autopilot is not engaged and there are not pilot inputs during the whole encounter. The LIDAR parameters correspond to a LIDAR set identified in [1] as a LIDAR set with comparably low requirements for the LIDAR sensor but good alleviation performance. The LIDAR sensor has 3 vertical and 3 lateral scan axes at 60 m ahead of the aircraft in a scan field-of-view of +/-10° in vertical and +/-16° in lateral direction. The field-of-view update rate of the nine measurement points in 10 Hz. The blur depth is 15 m.

It can be seen in FIG 10 that the wake impact alleviation in terms of bank angle reduction is very successful only for 45 to 60% of the altitude offsets tested. In other cases the maximum bank angle is not significantly reduced or even strongly increased in a few cases. The results of [1] gave the impression that this LIDAR parameter set provides adequate performance. The new results, however, show that the performance (with these LIDAR parameters) is quite sensitive to the encounter geometry and insufficiently robust.

In FIG 10, the left-most seven as well as the right-most three simulations correspond to case for which no or only little effects of the wake vortex was observable through the measurements (vortex too far below or above the aircraft flight path). In these cases, the wake identification algorithms was either never started or did not find a plausible result if started, cf. [1] for further details on the start criteria and on the plausibility checks. The fact that the system is not activated is not critical in these cases, since the influence of the wake vortex is low at these distances.

The next three cases as well as the encounter with an altitude offset of $\Delta H = 23\,\mathrm{m}$ case correspond to situations where the algorithm was started and found at least once a result that seemed plausible. In such a case the wake impact alleviation function uses that information, but it turns out that the information was not good enough and caused a deterioration of the aircraft reaction. Such cases are unacceptable and must be prevented.

The remaining cases show on average more than 50% improvement with negligible improvements or deteriorations in a few of these cases and some significant improvement in the majority of these cases. Even though the average performance is surprisingly good for the considered configuration, the irregularity in the alleviation performance is clearly unsatisfying.

For the parameter study in [1] and for the simulations shown in FIG 10 the LIDAR measurements that have been stored in the data buffer over the last 2 s are considered for the online wake identification. The value of 2 s was selected because it seemed to constitute a good tradeoff between computation time and adequate information about the wake vortex disturbance. An increase in data buffer capacity causes a proportional increase in the computation time required to evaluate the wake model outputs. Consequently, the wake characterization becomes computationally more expensive. Moreover, considering a large timeframe of LIDAR measurements also implies that many measurement locations are located outside the area where the wake vortex has a significant influence. Including many of these measurements without information of the wake vortex but only measurement noise can slightly impair the convergence to a good identification result.

For small encounter angles like the 5° lateral encounter, however, it turned out that considering measurements of the last 2 s only is too short. Due to the small encounter angle the wake vortex stays much longer in the field of view of the LIDAR sensor. Measurements older than 2 s thus still contain information about the wake vortex and would be beneficial to be included in the wake estimation process. FIG 11 shows the 5° lateral encounter for different wake altitudes when the data buffer of the OWIDIA system contains LIDAR measurements over the last 4 s. The blue dots in FIG 11 mark the maximum bank angle when the OWIDIA system is applied with the same LIDAR settings as shown in FIG 10 but with a data buffer containing measurements over 4 s. It can be noticed that wake impact alleviation is improved compared to the case when only measurement of 2 s are considered in the online wake identification. Nevertheless, there are still five altitude offsets between the wake vortex and the aircraft for which the OWIDIA system leads to an increase of the maximum bank angle. In five other cases, the alleviation performance is not very good. Nevertheless, in about 80% of the cases the alleviation performance is really good and certainly well beyond the expected results for this sensor configuration.

The green squares in FIG 11 denote the maximum bank angle which occurs during the wake encounter when LIDAR sensor with a higher spatial resolution is applied. This LIDAR sensor has 5 vertical and 7 lateral measurement directions. The field-of-view update rate for all 35 measurement stays at 10 Hz and the measurement range is also kept equal to 60 m. The field of view is increased to +/-10° in vertical and +/-30° in horizontal direction. The blur depth is 30 m. In this case the OWIDIA never aggravates the maximum bank, the evolution of the alleviation performance over the altitude range does not contain outliers anymore, and the achieved bank angle reduction is very significant.

For all wake vortex encounters presented so far, the wake vortex disturbance is modelled as an analytical Burnham-Hallock wake vortex (cf. section 3.1). Real wake vortices are possibly more complex, non-uniform, and can only partially be described with such a simplified model. A more representative way to model wake vortices is to compute the flow field using Large Eddy Simulations (LES) (cf. [20]). This approach can cover more details of the wake physics like wake deformation and decay. FIG 12 shows 5° lateral encounter with a LES wake vortex. The LES wake vortex is embedded in a three-dimensional field whose geometrical reference cannot easily be compared to the reference system used for the analytical vortex of FIG 10 and 11, leading to about 55 m altitude offset between these coordinates. The overall shape of the results shown in FIG 11 and 12 is nevertheless very similar and eases the comparison between these cases. In FIG 12, the simulated wake vortex has an age of 16 s, which is rather young for a wake vortex encounter but justified here by the fact that the results at this age shall be easier to compare with an analytical vortex because at this age the decay process has hardly begun and the two vortex centerlines are still relatively straight and parallel. Nevertheless the wake vortex differs from the analytical Burnham-Hallock model used inside the online wake identification process, which makes the identification possibly more challenging. The results shown in FIG 12 demonstrate, however, that even in this more challenging case of a more complex model of the wake vortex disturbance the OWIDIA performs very well.

When the OWIDIA system is applied with the lower resolution LIDAR sensor with 3 lateral and vertical measurement axes there are two cases in which the OWIDIA system aggravates the maximum bank angle. Note, however, that these two cases are relatively uncritical looking at the respective amplitudes. More importantly, the average alleviation performance on the other cases is still in the order of 60%, but nonetheless significantly worse than with the analytical Burham-Hallock wake vortex.

In the case of the higher resolution LIDAR sensor with 5 vertical and 7 lateral measurement axes, the OWIDIA system works very well for the LES wake vortex as well (see FIG 12). At all but two altitudes the maximum bank angle is impressively reduced (more than 65-70%, often even approximately 90%). The exception is for an altitude offset of $\Delta H = 30\,m$, for which only a slight improvement was achieved. The vortex impact in this case is very low and the vortex is also quite far from the sensor measurement zone. The wake encounters during which the wake alleviation was not activated only induced absolute bank angles lower than 5°. For both types of vortices (Burnham-Hallock in FIG 11 and LES in FIG 12) and for most altitude offsets, the bank angles are well below 5° when the OWIDIA system is applied, compared to maximum bank angles without OWIDIA of 20° or larger. The worst case was obtained with the LES wake vortex (FIG 12) at an altitude offset of 62.5 m. In this case the maximum bank angle did not exceed 11°, which is still a significant reduction compared to the 28° maximum absolute bank angle obtained in the same case without OWIDIA. Note also that with the 5x7 configuration the OWIDIA system is either active and very effective or not active due to insufficient information on the vortex (absolute altitude offset too large). No region with poor performance is observable at the boundary between these domains.

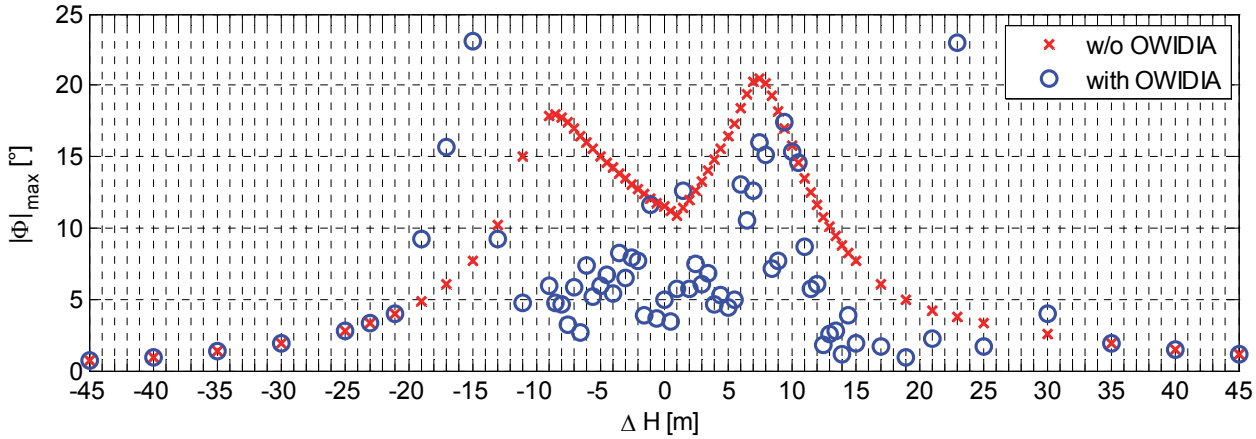

FIG 10: Reduction of maximum bank angle with OWIDIA using LIDAR sensor with a grid of 3x3 measurement points and a 2 s buffer for different wake altitudes. Lateral encounter angle is always 5°. Wake vortex model: Burnham-Hallock.

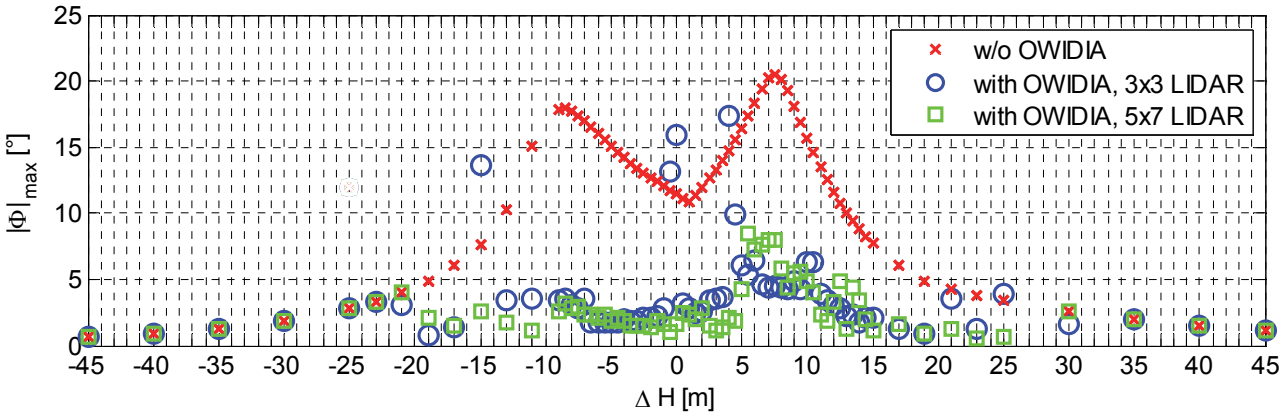

FIG 11: Reduction of maximum bank angle with OWIDIA with 4 s data buffer for different wake altitudes. Lateral encounter angle is always 5°. Wake vortex model: Burnham-Hallock. Blue circles: same sensor as in FIG 10 but with 4 s buffer. Green squares: sensor with higher spatial resolution (5x7 instead of 3x3) also with 4 s buffer.

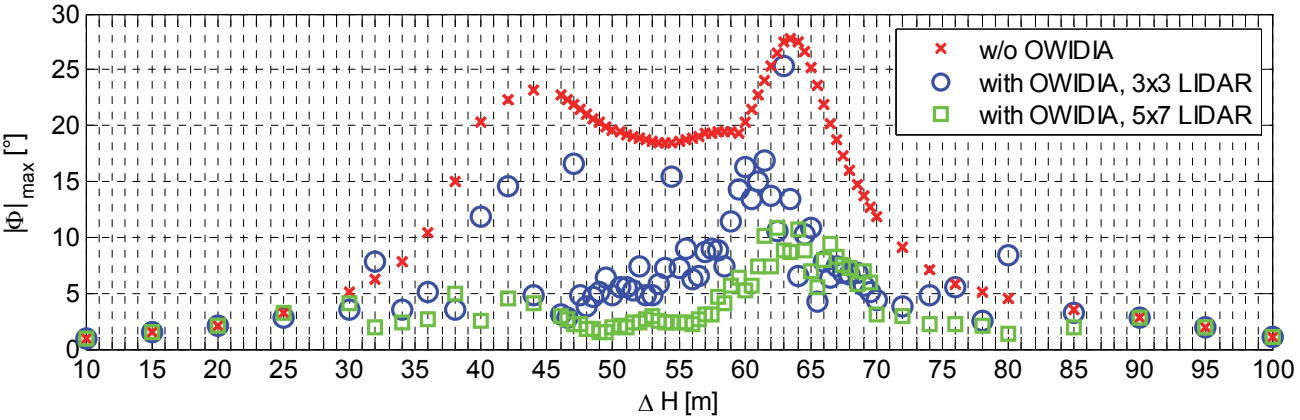

FIG 12: Reduction of maximum bank angle with OWIDIA with 4 s data buffer for encounter with 16-s-old LES wake vortex at different altitudes. Same sensor configurations as in FIG 11: only difference to FIG 10 is the wake model used.

There is a domain for which the alleviation performance is good but slightly worse than for other altitude offsets. Both LIDAR configurations exhibit this behavior in FIG 11 and 12. This effect shall be investigated further in future work. The respective altitude offset intervals are $\Delta H \in [4\,\mathrm{m}, 15\,\mathrm{m}]$ for the analytical vortex (FIG 11) and $\Delta H \in [59\,\mathrm{m}, 70\,\mathrm{m}]$ for the LES vortex (FIG 12). Even in these intervals, for which further improvements might be possible, the current minimum alleviation performance obtained was still a reduction of 50% of the maximum bank angle. The performance of the OWIDIA system should also be assessed for older LES vortices with stronger deformation. The current identification model provides no parameters for wake deformation. Therefore, it is expected that for strongly deformed vortices the model will have to be extended.

To summarize the results on the wake vortex application it can be stated that they are also very good. The use of remote wind sensors with the Online Wake IDentification and Impact Alleviation creates a very large potential for safety and air traffic capacity improvement.

5. NEED FOR FLIGHT DEMONSTRATION

As it can be seen in the results shown previously, in-flight remote sensing of line-of-sight velocity components (e.g. Doppler LIDAR) can provide useful information, even if the line-of-sight velocity components are not directly the components that contain the most important information on the considered phenomena. Two quite different applications but using the same type of sensors and the same ideas in terms of measurement post-processing were shown, which illustrates the strong commonality between these applications. The results shown are just some examples among others, which all show the remarkable potential for the onboard remote wind sensing technologies. In addition to these two applications (gust/turbulence load alleviation and wake impact alleviation), other applications using these sensors e.g. to increase air data redundancy may also be very interesting.

However, even though there are many attractive applications for these technologies, all these applications are distinct enough to be often investigated within different projects/frameworks. For instance, most research activities for active load alleviation are based on airframe research fundings (e.g. CleanSky SFWA-ITD and CleanSky 2 Airframe-ITD). Research activities on wake vortex (encounter prevention measures, impact alleviation) are mainly based on air transportation research funds (e.g. SESAR 1 & 2).

This makes it difficult to develop and exploit the synergies between the different potential applications on the remote sensing technologies and to reach the critical funding size to perform maturation activities and in-flight demonstrations. Maturation activities, for instance developing good airframe integration concepts (with respect to aerodynamics, window heating, instrument cooling, etc.), are needed to make the step from research instruments to real prototypes.

Flight demonstration is also required to characterize the capability of these sensors to cope with all kinds of atmospheric conditions (low aerosol concentrations, water drops, ice, etc.) and to demonstrate the capacity of the post-processing algorithms to characterize real-world gust and turbulence fields or strongly deformed wake vortices well enough for the purpose of the corresponding alleviation functions. Such demonstrations are required to permit the evaluation of the level of reliability that can be reached for the whole system and for the targeted applications. Reliability is crucial for aeronautical systems and the conditions that are needed to test the remote sensing technologies cannot, to the best of the authors' knowledge, be reproduced currently in a ground-based testing environment.

6. CONCLUSIONS

Two applications of in-flight remote wind sensing technologies were presented in this paper. The first application considers the use of this technology for the recognition of gusts and turbulence, with the aim of using this information for active load alleviation. In the second application the measurements support the characterization of wake vortices. The knowledge gained on the wake vortices permits to alleviate the impact of this phenomenon on the aircraft and thereby to increase the safety. The paper focused on the remote sensing and measurement processing and showed the strong similarities between the post-processing algorithms that are needed for both applications. The achieved and presented results for both applications are very good. The reconstructed wind profiles are clearly good enough to enable their use for active load alleviation. In the wake vortex case, the wake characterization is already integrated into the wake impact alleviation control system and the results showed reductions of the maximum bank angle up to 92% and between 75 and 90% in the large majority of the cases for the preferred sensor settings. Further maturation of both systems shall be performed in the near future. Various uncertainties on the technology and on some assumptions underlying the post-processing algorithms should be verified with real data (e.g. collected in flight). Later on in-flight demonstration of the complete systems (including alleviation) should be performed.

7. REFERENCES

[1] Ehlers, J., Fezans, N., *Airborne Doppler LiDAR Sensor Parameter Analysis for Wake Vortex Impact Alleviation Purposes*, Chapter in book: *Advances in Aerospace Guidance, Navigation and Control*, Springer, pp. 433-453, Toulouse, April 2015. ISBN 978-3-319-17517-1.

[2] Cézard, N., Besson, C., Dolfi-Bouteyre, A., Lombard, L., *Airflow Characterization by Rayleigh-Mie Lidars*, AerospaceLab, Issue 1, Dec. 2009.

[3] Hill, C., Harris, M., *Lidar measurement report*, Technical report: Remote Sensing (UpWind WP6) – QinetiQ Lidar Measurement Report, Sept. 2010, (QINETIQ/ TS/ FPPS/ TR0900813).

[4] NATO, *Optical Air Flow Measurement in Flight*, RTO AGARDograph 160, Flight Test Instrumentation Series – Vol. 20, Dec. 2003.

[5] Wolkensinger, C., *Vergleich messtechnischer Konzepte zur bordgestützten Ermittlung atmosphärischer Störphänomene* (English title: Comparison of measurement concepts for the detection of atmospheric disturbances), DLR Technical Report IB-111/2010-35, 2010.

[6] Hirschberger, M. C., *Beiträge zur Erfassung von Wirbelschleppen mit Lidar – Simulation und Analyse rückgestreuter Signale zur Windfeldbestimmung vor Flugzeugen* (English title: Contribution to the

recognition of wake vortices with Lidar – Simulation and analysis of backscattered signals for the wind field determination ahead of aircraft), PhD thesis, Ludwig-Maximilian University, Munich, 2013.

[7] Sivia, D. S., *Data Analysis – A Bayesian Tutorial*, Oxford University Press, 2nd Edition, ISBN-13: 978-0198568315, July 2006.

[8] Gregory, P., *Bayesian Logical Data Analysis for the Physical Sciences*, Cambridge University Press, ISBN-13: 978-0-521-84150-4, 2005.

[9] Burnham, D. C., Hallock, J. N., *Chicago Monostatic Acoustic Vortex Sensing System, Vol. 4, Wake Vortex Decay*, National Information Service, Springfield, VA, 1982.

[10] Lamb, H., *Hydrodynamics*, New York, Dover Publications, ISBN-13 of 6th edition: 978-0486602561, 1932.

[11] Proctor, F. H., Hamilton, D. W., *Evaluation of Fast-Time Wake Vortex Prediction Models*, AIAA-2009-0344, AIAA Aerospace Sciences Meeting, Orlando, FL, USA, January 2009.

[12] Winckelmans, G., Thirifay, F., Ploumhans, P., *Effect of non-uniform wind shear onto vortex wakes: parametric models for operational systems and comparison with CFD studies*, 4th Wakenet Workshop on "Wake Vortex Encounter", NLR, Amsterdam, The Netherlands, October 16-17th, 2000.

[13] Fabre, D., Jacquin, L. *Short-wave cooperative instabilities in representative aircraft vortices*, AIP Physics of Fluids, Vol. 16, No. 5, pp. 1366-1378, May 2004.

[14] Luckner, R., *Modeling and Simulation of Wake Vortex Encounters: State-of-the-Art and Challenges*, AIAA-2012-4633, AIAA Modeling and Simulation Technologies Conference, Minneapolis, MN, USA, August 2012.

[15] Fischenberg, D. *Determination of Wake Vortex Characteristics from Flight Test Data* (in German: *Bestimmung der Wirbelschleppencharakteristik aus Flugmessdaten*), DLRK / Deutscher Luft- und Raumfahrtkongress, Stuttgart, 23rd - 26th Sept. 2002.

[16] Fischenberg, D., *A method to validate wake vortex encounter models from flight test data*, ICAS 2010, 27th International Congress of the Aeronautical Sciences, Nice, France, 2010.

[17] Fraley, C., *Algorithms for Nonlinear Least-Squares Problems*, Technical Report DTIC: ADA196071, May 1988.

[18] Crow, S. C., *Stability Theory for a Pair of Trailing Vortices*, AIAA Journal, Vol. 8, No 12, pp 2172-2179, 1970.

[19] Crow, S. C., Bate, E. R., *Lifespan of Trailing Vortices in a Turbulent Atmosphere*, Journal of Aircraft, Vol. 13, No. 7, pp. 476-482, 1976.

[20] Hennemann, I., *Deformation und Zerfall von Flugzeugwirbelschleppen in turbulenter und stabil geschichteter Atmosphäre* (English title: Deformation and decay of aircraft wake vortices in turbulent and stable atmosphere), PhD thesis, Technische Universität München, Germany, 2009.

[21] Loucel, R. E., Crouch, J. D., *Flight-Simulation Study of Airplane Encounters with Perturbed Trailing Vortices*, Journal of Aircraft, Vol. 42, No. 4, pp. 924-931, July-August 2005.

[22] Bieniek, D., Luckner, R., *Simulation of Aircraft Encounters with Perturbed Vortices Considering Unsteady Aerodynamic Effects*, Journal of Aircraft, Vol. 51, No. 3, May-June 2014.

[23] Vechtel, D., *Entwicklung eines analytischen Modells zur Berechnung gekrümmter Wirbelschleppen*, DLR Technical Report IB 111-2010/14, Braunschweig, March 2010

[24] Münster, C., *Modellierung, Identifizierung und Bewertung eines analytischen Modells für gekrümmte Wirbelschleppen* (English title: Modeling, Identification, and Evaluation of an Analytical Model of Curved Vortices), DLR Technical Report IB-111-2011/09, Braunschweig, March 2011.

[25] Marr, D., Hildreth, E., *Theory of Edge Detection*, Proceedings of the Royal Society of London. Series B, Biological Sciences, Vol. 207, No. 1167, pp. 187-217, Feb. 1980.

[26] König, R., Hahn, K.-U., *Load Alleviation and Ride Smoothing Investigations Using ATTAS*. In Proceedings of the 17th Congress of the International Council of the Aeronautical Sciences, Stockholm, Sweden, 1990.

[27] Hahn, K.-U., König, R., *ATTAS Flight Test and Simulation Results of the Advanced Gust Management System LARS*. Proc. of the AIAA Atmospheric Flight Mechanics Conference, Hilton Head, SC, USA, 1992.

[28] König, R., Hahn, K.-U., Winter, J., *Advanced Gust Management Systems - Lessons Learned and Perspectives*. In AGARD Flight Mechanics Panel, Symposium on Active Control Technology: Applications and Lessons Learned, Torino, Italy, 1994.

[29] Schmitt, N. P., et al., *The AWIATOR Airborne LIDAR Turbulence Sensor*, DLRK / Deutscher Luft- und Raumfahrtkongress 2005, Friedrichshafen, DGLR-2005-067, September 2005.

[30] Hecker, S., Hahn, K.-U., *Gust Load Alleviation System using turbulence sensor and adaptive elements*. AWIATOR, Technical Report, DLR-TR-3.1.1-14, Germany, July 2006.

[31] Wildscheck, A., *An Adaptive Feed-Forward Controller for Active Wing Bending Vibration Alleviation on Large Transport Aircraft*. PhD thesis, Technical University of Munich, 2008.

[32] European Aviation Safety Agency, *Certification Specifications for Large Aeroplanes*, CS 25, Amendment 3, Sept. 19th 2007, Annex to ED Decision 2007/010/R.

[33] Fischenberg, D., *Online Wake Identification Algorithms Using Forward Looking LIDAR Sensor Measurements*, DLR Technical Report IB111-2013/11 Braunschweig, Germany, February 2013.

[34] Fischenberg, D., *Strömungsermittlungsverfahren/ Flow Determination Method/Procédé de détermination d'écoulement*, Patent No. EP 2 340 438 B1, European Patent Office 2013; Patent No. US 9075074 B2, United States Patent and Trademark Office 2015.

[35] Ehlers, J., Fischenberg, D., Niedermeier, D., *Wake Identification Based Wake Impact Alleviation Control*, AIAA-2014-2591, AIAA AVIATION, Atlanta, GA, USA, June 2014.